Research Square

Preprints are preliminary reports that have not undergone peer review.
They should not be considered conclusive, used to inform clinical practice,
or referenced by the media as validated information.

Integrative Transcriptomic and Radiogenomic Analysis Identifies a MAPT-PC-GLUD1 Low-Signature State in Glioblastoma

Xuhang Yang
Wenzhou Medical University
Zhe Wu
Wenzhou Medical University
Chencheng Lv
Wenzhou Medical University
Donhao Qin
Wenzhou Medical University
Yutuo Zheng
Wenzhou Medical University
Jian Lin
linjian3222@wmu.edu.cn
Wenzhou Medical University

Research Article

Keywords: Glioblastoma, Radiogenomics, MAPT-PC-GLUD1 signature, Low-signature state, Tumor heterogeneity, Immune microenvironment, Multi-omics integration

Posted Date: June 5th, 2026

DOI: https://doi.org/10.21203/rs.3.rs-9666973/v1

License: This work is licensed under a Creative Commons Attribution 4.0 International License.
Read Full License

Additional Declarations: No competing interests reported.

Abstract

Glioblastoma (GBM) is characterized by marked molecular, cellular, and spatial heterogeneity, which contributes to therapeutic resistance and poor clinical outcomes. Although metabolic adaptation and ribosome biogenesis are both central to GBM biology, it remains unclear whether a compact transcriptional state linking these programs can be connected to immune contexture, cellular heterogeneity, and MRI-visible imaging phenotypes. We developed an integrative multi-omics and radiogenomic framework to identify a biologically interpretable gene signature associated with GBM heterogeneity and prognosis. Candidate genes were screened from public GBM transcriptomic datasets by differential expression analysis, weighted gene co-expression network analysis, and machine learning-based feature selection. Associations with survival, clinicopathological variables, immune characteristics, genomic features, methylation, and single-cell expression patterns were systematically evaluated. MRI-based radiomic features from 92 patients with matched transcriptomic data were used to construct exploratory predictive models, and voxel-wise maps were generated to visualize imaging-derived intratumoral heterogeneity. We identified a three-gene signature composed of MAPT, PC, and GLUD1. Lower expression of this signature defined a low-signature state associated with worse survival, unfavorable molecular features, higher tumor mutational burden, and a more immunoregulatory tumor microenvironment. Single-cell analysis revealed cell-type-specific expression heterogeneity, whereas radiomic models showed moderate performance in estimating gene-associated imaging signatures. Exploratory pharmacogenomic and molecular docking analyses suggested candidate compounds for further investigation. Together, these findings define a MAPT-PC-GLUD1 low-signature state that links metabolic-cellular programs with immune regulation, malignant progression, and MRI-derived spatial heterogeneity. Rather than serving merely as a prognostic model, this signature provides a biologically interpretable radiogenomic axis for future translational studies in GBM.

Introduction

The most prevalent and lethal primary brain tumor is glioblastoma (GBM), which is a WHO grade IV malignancy [1]. Although surgical resection and adjuvant therapies have improved over the last decades, patient survival has not improved greatly, leading to poor clinical outcomes [2–4]. This frequent failure of treatment has been significantly contributed to by the biological features of GBM, including high intratumoral heterogeneity, rapid growth, invasion into the surrounding brain tissue, and resistance to radiation and chemotherapy [5–7]. Therefore, even aggressive multimodal therapies can hardly maintain disease control, and recurrence is almost inevitable [8].

Metabolic reprogramming is a characteristic of GBM. Tumor cells have to adapt strongly to bioenergetic conditions in order to survive and proliferate in unfavorable microenvironmental conditions. GBM cells selectively use aerobic glycolysis, thus redirecting metabolic intermediates into biosynthetic pathways that are necessary for the production of nucleotides and amino acids [9–11]. At the same time, glutamine metabolism facilitates anabolic needs and redox homeostasis, maintaining tumor growth during stress [12–13]. Enhanced ribosome biogenesis (RiBi) also promotes effective accumulation of

biomass, as it helps to maintain protein synthesis in fast-dividing GBM cells. Oncogenic signaling, such as c-MYC and mTOR signaling, controls this process [14–16]. Nevertheless, too much RiBi stimulation may lead to ribosomal stress, which causes p53-dependent growth arrest or apoptosis [17], indicating that RiBi is both a growth-promoting factor and a possible weakness in GBM.

The processes of metabolic reprogramming and RiBi are closely interconnected, not independent. Metabolic pathways supply the energy and substrates needed for the production of ribosomes, and high RiBi levels can increase metabolic enzyme translation. The coordination of this bidirectional relationship is achieved through signaling pathways including mTOR, AMPK, and HIF-1α, which integrate nutrient and oxygen availability [9, 20–21]. Changes in this relationship probably cause the metabolic plasticity and heterogeneity that are typical of GBM [13, 22–24].

Although these insights have been made, there are a number of critical gaps that have not been addressed. To start with, molecular programs that integrate metabolic adaptation with biosynthetic stress in GBM have not been adequately reduced into small and understandable signatures. Second, the majority of transcriptomic features based on bulk-type data do not consider the cellular-state heterogeneity of the GBM ecosystem. Third, therapeutic approaches based on metabolism or ribosome biogenesis themselves have not been effective clinically, implying the need for an integrated framework to link molecular programs to tumor behavior, immune regulation, and clinically accessible phenotypes.

Radiogenomics is an exciting non-invasive methodology to match molecular changes to imaging phenotypes. Quantitative MRI data can be analyzed using machine learning to infer genomic and transcriptomic characteristics from imaging data [26–27]. This method has been applied in GBM to forecast clinically relevant molecular features, including MGMT promoter methylation status and IDH mutation status, as well as the tumor immune microenvironment and patient prognosis [28–33]. However, the majority of radiogenomic analyses have concentrated on discrete molecular factors or general survival data, but fewer studies have tried to map functionally coordinated transcriptional programmes to spatially varied imaging phenotypes.

To fill these gaps, we created an integrative multi-omics and MRI radiogenomic system to examine and define a small signature based on metabolism- and ribosome biogenesis-related candidate genes. We determined a MAPT-PC-GLUD1 signature and assessed its correlations with prognosis, clinicomolecular, immune contexture, and genomic variables, single-cell expression patterns, and MRI-based spatial heterogeneity. This research connects a biologically interpretable transcriptional state to non-invasive imaging characteristics and proposes a hypothesis-generating framework to create biomarkers and explore future therapies in GBM.

Methods

Data Acquisition and Preprocessing

Publicly available multi-omics datasets were collected and organized according to the analytical workflow of this study. The GEO dataset GSE4290 (63 GBM and 23 non-tumor brain samples; Affymetrix GPL570 platform) was used as the primary GBM discovery cohort for differential expression and co-expression network analyses, while GSE116520 served as an independent external validation cohort for the machine learning-based feature selection workflow. To further assess the clinical and prognostic relevance of the identified signature, transcriptomic and clinical data from TCGA and CGGA were additionally included. Accordingly, the main discovery analyses were performed in GBM-focused datasets, whereas subsequent validation analyses were extended to glioma cohorts when clinicopathological variables across tumor grades and molecular subtypes were evaluated. For radiogenomic analysis, we retrospectively collected data from TCGA and CGGA, and a total of 92 GBM patients with matched preoperative T1-weighted contrast-enhanced (T1ce) MRI sequences and transcriptomic profiles were included to develop imaging-based models for estimating the status of the identified gene-associated signature. Gene sets associated with RiBi and metabolism were obtained from the GeneCards database based on relevance scores, and genes with a relevance score greater than 1 were included for further analysis. RNA-seq expression profiles, microsatellite instability (MSI) data, tumor mutational burden (TMB) data, and mutation-related information were retrieved from the Genomic Data Commons (GDC) portal, and downstream analyses were performed on expression data transformed as $\log_2(\text{TPM} + 1)$.

Differential Expression and Integrative Functional Analysis

Principal component analysis (PCA) was initially performed to assess the sample distribution and data quality in the discovery cohort (GSE4290). The Limma R package was then used to perform differential expression analysis, with thresholds of $\log_2$ fold change greater than 0.5 and FDR less than 0.05, and the results were visualized using standard R packages. To narrow down genes potentially related to metabolic reprogramming and RiBi, differentially expressed genes were intersected with curated gene sets, resulting in 349 candidate genes. ClusterProfiler was then used to perform functional enrichment analyses, including Gene Ontology (GO) and KEGG pathway analyses, with an FDR threshold of 0.05. Gene Set Enrichment Analysis (GSEA) was conducted using MSigDB v2023.2 C2 curated gene sets with 1,000 permutations, and pathways with FDR < 0.25 and NES > 1 were regarded as significant. Gene Set Variation Analysis (GSVA) was used in parallel to determine pathway activity at the sample level. A weighted gene co-expression network analysis (WGCNA) was subsequently conducted to obtain modules related to metabolic and ribosome biogenesis phenotypes, based on which 62 hub genes were selected according to module–trait relationships for further analysis.

Prognostic Clustering and Machine Learning-based Feature Selection

To explore survival-associated molecular heterogeneity in GBM, LASSO Cox regression analysis was first performed on the 349 candidate genes in the discovery cohort, resulting in 25 genes associated with overall survival. Based on these genes, unsupervised consensus clustering was conducted to stratify patients into molecular subtypes, which was further supported by PCA. To construct a more stable

prognostic model, the 62 hub genes identified by WGCNA were subsequently subjected to machine learning-based feature selection. LASSO regression was first applied to reduce dimensionality and eliminate redundant variables, followed by Random Forest (RF) and Support Vector Machine–Recursive Feature Elimination (SVM-RFE) with 10-fold cross-validation to improve the robustness of feature selection. Genes consistently retained across these methods were considered the most robust candidates for downstream prioritization. Their chromosomal distribution was then examined, and the final retained genes were used for subsequent biological, clinical, and radiogenomic analyses.

Clinical Evaluation and Prognostic Validation

TCGA glioma cohorts were used to evaluate the prognostic associations of the final three-gene signature. For analyses of individual signature genes, patients were divided into high- and low-expression groups according to the median expression value of each gene. Kaplan–Meier survival analysis and the log-rank test were used to compare overall survival between groups. Predictive performance was assessed using time-dependent receiver operating characteristic (ROC) curves at 1, 3, and 5 years. Decision curve analysis (DCA) was additionally performed as an exploratory evaluation of model performance across threshold probabilities.

Multi-omics Integration and Tumor Microenvironment Characterization

To describe the tumor microenvironment, immune cell infiltration was estimated using the immunedeconv framework, a widely applicable collection of deconvolution approaches. The expression of major immune checkpoint genes, including IDO1, ICOS, TIGIT, CD274, CD28, CTLA4, and LAG3, was also analyzed, and the Tumor Immune Dysfunction and Exclusion (TIDE) algorithm was used to predict possible responses to immune checkpoint blockade. Moreover, Spearman correlation analysis was used to examine the correlations between the final three-gene signature and immune-related features, such as immune cell infiltration, checkpoint expression, stemness index (mRNAsi), MSI, and TMB. For single-cell analysis, the scRNA-seq data (GSE84465; TISCH database) were processed using standard workflows in Seurat and MAESTRO, including normalization, quality control, and dimensionality reduction, and t-SNE was employed to visualize cell clusters and assess the expression patterns of specific cell types. The promoter DNA methylation levels of the signature genes in the TCGA glioma cohort were also investigated using the UALCAN platform.

Radiomics Feature Extraction and Predictive Model Construction

Among the 92 patients with matched transcriptomic data and preoperative contrast-enhanced T1-weighted MRI (T1CE) images, tumor regions of interest (ROIs) were manually defined. Two senior radiologists performed blinded segmentation using ITK-SNAP (v4.10.2), and discrepancies were resolved by consensus. Before feature extraction, all T1CE images were preprocessed using N4 bias field correction and resampled to an isotropic voxel size of $1 \times 1 \times 1$ mm^3 to improve consistency across datasets. Radiomic features were then extracted and normalized using z-score transformation. For voxel-based radiogenomic analysis, SimpleITK was used to process MRI images and segmentation

masks, and 3D bounding box cropping was implemented to reduce computational load. Wavelet decomposition and Laplacian of Gaussian (LoG) filters were applied to obtain multi-scale imaging features, and PyRadiomics was used to extract voxel-wise radiomic features under standardized conditions, including first-order statistics and texture features such as GLCM, GLSZM, GLRLM, and GLDM. LASSO regression was subsequently used to reduce feature redundancy and select informative features for model construction, and the dataset was randomly divided into training and validation cohorts at a ratio of 7:3. To evaluate predictive performance, several widely used machine learning models, including tree-based and neural network models, were tested, and ROC curves, area under the curve (AUC), and DCA were used to assess model performance in the internal validation cohort. These models were used as exploratory predictors of gene-associated imaging signatures rather than clinically validated diagnostic tools. Finally, voxel-based features were combined with model-derived coefficients to generate spatial prediction maps, which were used to visualize molecular signature-associated imaging patterns within tumors and to provide an approximation of intratumoral heterogeneity through an imaging-based approach. Representative outputs included MRI overlays and voxel-wise feature distributions, and these maps were interpreted as imaging-derived surrogate maps rather than direct spatial measurements of gene expression.

Drug Sensitivity Analysis and Molecular Docking

Data from the Genomics of Drug Sensitivity in Cancer (GDSC) database were used to assess the associations between the expression of hub genes (GLUD1, PC, and MAPT) and drug response. Drug sensitivity was evaluated using IC50 and AUC values in cancer cell lines, and these relationships were tested by Spearman correlation analysis with P values adjusted using the Benjamini–Hochberg method. For molecular docking analysis, protein structures were retrieved from the Protein Data Bank (PDB), and candidate compounds, including Navitoclax and WH-4-023, were subjected to standard preprocessing procedures. Docking simulations were performed using AutoDock Vina, and binding affinities were compared on the basis of predicted binding energies. Protein–ligand interaction images were generated using PyMOL.

Statistical Analysis

All statistical analyses were performed using R software (v4.5.2). Data distribution was assessed before analysis, and necessary non-parametric tests (Mann-Whitney U test or Kruskal-Wallis test) were used. All tests were two-sided, and $P < 0.05$ was considered statistically significant. Standard R packages were used for data visualization.

Results

Identification of candidate genes associated with metabolism, ribosome biogenesis, and prognosis

Differential expression analysis comparing GBM and normal brain tissues identified 5,757 differentially expressed genes (DEGs), indicating marked transcriptional differences between tumor and normal

tissues (Figures 2A–C). To further focus on genes associated with metabolic reprogramming and RiBi, these DEGs were intersected with curated gene sets, yielding 349 candidate genes (Figure 2D). Functional enrichment analysis showed that these genes were involved in multiple tumor-related biological processes and pathways, including cell cycle regulation, apoptosis, glioma-related signaling, as well as metabolic and ribosome biogenesis pathways (Figures 2E–F), suggesting a potential link between metabolism and RiBi in GBM. To further evaluate their prognostic relevance, LASSO Cox regression analysis identified 25 genes associated with overall survival (Figure 2G), and this prognostically relevant gene set stratified patients into groups with significantly different survival outcomes (Figures 2H–I). These findings provided an initial basis for the subsequent integrative prioritization of prognostically informative candidates.

Identification and Biological/Immunological Differences of Molecular Subgroups

To further characterize the biological heterogeneity represented by the prognostically relevant candidate gene set, unsupervised clustering based on the 25 selected genes classified patients into two molecular subtypes, C1 and C2, which were clearly separable by PCA (Figures 2J–M). Survival analysis showed that patients in the C2 subgroup had significantly poorer overall survival than those in C1 (Figure 2N). GSEA further revealed that the C2 subtype was characterized by enrichment of immune-regulatory and cellular senescence-related pathways, together with downregulation of several metabolic processes (Figure 3A). Consistently, immune infiltration analysis demonstrated marked differences in tumor microenvironment composition between the two subtypes: compared with C1, which showed relatively higher abundance of pro-inflammatory immune cells such as M1 macrophages, C2 was associated with increased infiltration of $CD8^+$ T cells, regulatory T cells (Tregs), M2 macrophages, and plasma cells (Figures 3B, 3E). In addition, several immune checkpoint molecules, including PD-1, CTLA-4, and TIGIT, were more highly expressed in C2 tumors (Figure 3F), and the C2 subgroup also exhibited higher TIDE scores, a higher stemness index, and a positive association with TIDE scores (Figures 3C–D). Clinically, patients in the C2 subgroup were older and more likely to have received radiotherapy, whereas other clinical variables did not differ significantly between the two subtypes (Figure 3G). Together, these findings indicate that the prognostically relevant candidate gene set captures biologically, immunologically, and clinically meaningful heterogeneity in GBM and provides a basis for subsequent integrative prioritization of the final hub genes.

Identification of Final Hub Genes Through Network Analysis and Machine Learning

To derive a smaller and biologically interpretable signature for downstream analyses, we integrated co-expression network analysis with machine learning-based feature prioritization. WGCNA was performed to construct a gene co-expression network and identify modules associated with GBM, and a soft-thresholding power of 6 was selected to achieve scale-free topology (Figures 3H, 3J). Module–trait correlation analysis showed that the blue module was most strongly associated with the GBM phenotype (Figure 3I). Within this module, correlation analysis further demonstrated a strong positive relationship between module membership and gene significance ($r = 0.88$, $P < 0.001$; Figure 3L).

Functional enrichment analysis of blue-module genes revealed enrichment in multiple tumor-related pathways, including cell cycle regulation, WNT/β-catenin signaling, and PI3K–AKT–mTOR signaling, together with decreased activity of apoptosis-related and p53-related pathways (Figure 3K). Overlap between genes in the blue module and the previously identified DEGs yielded 62 candidate genes for further prioritization (Figure 3M). To refine this candidate set, machine learning-based feature selection was subsequently performed: SVM-RFE identified 31 genes with consistently high classification performance, whereas random forest highlighted a smaller subset of genes with higher feature importance (Figures 4A–B). Genes retained by both approaches were considered the most robust candidates, leading to the identification of three final hub genes, GLUD1, PC, and MAPT (Figure 4C). Chromosomal mapping showed that these genes are located at 10q23.2 (GLUD1), 11q13.2 (PC), and 17q21.31 (MAPT) (Figure 4D). These three genes were therefore retained as the final hub-gene signature for all subsequent biological, clinical, and radiogenomic analyses.

Spatial Expression, Genomic, and Immune Correlates of the Final Hub Genes

Single-cell RNA sequencing data were used to characterize the expression patterns of the final hub genes GLUD1, PC, and MAPT. GLUD1 and PC were mainly localized to astrocyte-like malignant cells, whereas their expression was comparatively low in most other cell populations (Figures 4E and 4G). In contrast, MAPT showed higher expression in neuronal clusters, although it was also detectable in a subset of tumor cells (Figure 4F), suggesting that the three hub genes may reflect distinct cellular states within the glioma microenvironment. Genomic feature analysis did not reveal a clear association between hub-gene expression and MSI (Figure 5A), whereas TMB was negatively correlated with the expression of all three genes (Figure 5B). DNA methylation analysis showed only weak correlations with gene expression, and CpG-level analysis did not identify significant associations with survival outcomes (Figures 5C–E). Immune profiling further demonstrated differences in immune cell infiltration across expression groups (Figures 6A–C): higher expression of GLUD1 and PC was associated with greater infiltration of macrophages and activated natural killer (NK) cells, together with lower proportions of Tregs, whereas reduced MAPT expression was associated with increased CD8+ T-cell infiltration and higher expression of immune-related signatures. Several immune checkpoint molecules, including CD274 (PD-L1), CTLA4, LAG3, TIGIT, CD47, ICOS, CD28, and IDO1, were also more highly expressed in the low-expression groups (Figure 6D).

Clinical Relevance and Prognostic Value of the MAPT-PC-GLUD1 Low-Signature State

To further define the biological and clinical relevance of the MAPT-PC-GLUD1 signature, we systematically compared the expression patterns and prognostic performance of GLUD1, MAPT, and PC in glioma cohorts. Each of the three genes was expressed at significantly lower levels in glioma samples than in normal brain tissues and decreased steadily with increasing WHO grade, with the lowest expression levels observed in grade IV tumors (Fig. 7A, C), implying that loss of expression of this signature may be a hallmark of a low-signature state related to malignant progression. Since these genes were differentially expressed between glioma and normal tissues, diagnostic performance was

also evaluated, with MAPT showing the highest discriminatory ability, with an AUC of 0.841, followed by PC and GLUD1 (Fig. 7B). Although time-dependent ROC analysis for 1-year overall survival indicated that GLUD1, MAPT, and PC had AUC values of less than 0.5, specifically 0.153, 0.183, and 0.207, respectively (Fig. 7M), this trend suggested an inverse relationship between risk definition and gene expression, as observed in subsequent analyses, in which higher gene expression was associated with better survival. Decreased GLUD1, MAPT, and PC expression was also consistently linked with adverse molecular features, such as IDH wild-type status and 1p/19q non-codeletion (Fig. 7D-F), as well as poor clinical outcomes, as patients with adverse events typically had lower GLUD1, MAPT, and PC expression (Fig. 7G-I). In line with this, Kaplan-Meier analysis revealed that overall survival was significantly improved in patients with higher expression of GLUD1, MAPT, and PC, and Cox proportional hazards analysis further demonstrated their protective associations, with hazard ratios between 0.17 and 0.28 (all $P < 0.001$; Fig. 7K). Heatmap analysis provided an overview of these associations and confirmed that the three genes were reduced in tumors with increasing WHO grade, IDH wild-type status, 1p/19q non-codeletion, and age over 60 years (Fig. 7J), supporting the close association between the three-gene signature and aggressive clinicopathological features. Lastly, a nomogram using the gene signature and clinicopathological variables to predict individual prognosis was developed, with calibration curves indicating excellent concordance between the predicted and observed survival rates at 1, 3, and 5 years (Fig. 7L), and decision curve analysis indicated a net benefit across a range of specific threshold probabilities, particularly when long-term survival prediction was required (Fig. 7N). Taken together, these results indicate that GLUD1, MAPT, and PC may serve as protective glioma-associated genes and that their low expression may define a clinically adverse low-signature state, although further validation in external cohorts is needed.

Exploratory Voxel-level Radiogenomic Mapping and Model Feature Analysis

Radiomics models were developed using PC-, GLUD1-, and MAPT-related feature sets to evaluate whether MRI-derived phenotypes could serve as exploratory surrogates for molecularly associated signatures. After dimensionality reduction by LASSO regression, a small set of representative non-zero features was retained in each model for further analysis (Fig. 8A, F, K). These selected features were mainly associated with gray-level heterogeneity, local textural complexity, dependence, and run-length properties (Fig. 8B, G, L), suggesting that imaging phenotypes linked to the MAPT-PC-GLUD1 axis were primarily reflected by intralesional textural patterns rather than global morphology alone. Voxel-wise feature maps further revealed marked spatial heterogeneity in the most important PC-, GLUD1-, and MAPT-related radiomic features within lesions (Fig. 8C, H, M), indicating that predictive information was distributed spatially within tumors rather than being limited to global morphologic variation. Four machine learning classifiers, including K-nearest neighbor (KNN), multilayer perceptron (MLP), random forest (RF), and extreme gradient boosting (XGBoost), were then built and tested in the training and validation cohorts using the selected features (Fig. 8D, I, N). Overall, all three molecularly associated radiomics signatures demonstrated excellent discriminatory ability in the training cohort and retained moderate predictive capacity in the validation cohort. In the PC-related model, each classifier showed discriminatory value in the validation cohort, with KNN achieving the best AUC of 0.791 (95% CI, 0.623–

0.959). The validation performance of the GLUD1-related model was also lower than that in the training cohort, but the models still retained basic predictive information, indicating that GLUD1-associated radiomic features may still contain some predictive value. RF demonstrated the best validation performance in the MAPT-related model, with an AUC of 0.769 (95% CI, 0.595–0.942), and the other two models, XGBoost and KNN, demonstrated moderate discriminatory ability, indicating that the validation performance of the MAPT-associated radiomic signature was relatively stable. These three molecularly linked radiomic signatures, in combination, showed exploratory predictive ability, with the PC-related model showing the most robust validation performance in the validation cohort and the MAPT-related model displaying relatively better overall validation performance. Decision curve analysis also showed that some models provided a higher net benefit than both the treat-all and treat-none strategies within certain probability ranges (Fig. 8E, J, O), particularly RF and XGBoost, suggesting their potential value in the development of imaging-based risk stratification models rather than direct clinical decision-making.

Drug Sensitivity and Molecular Docking Evaluations

Drug sensitivity was evaluated using GDSC data, and compounds related to the expression of hub genes were identified. A total of 30 compounds were significantly associated with hub-gene expression (FDR ≤ 0.05; Figure 9A). Among them, Navitoclax and WH-4-023 were selected for further analysis due to their similar associations with gene expression. In particular, sensitivity to Navitoclax was correlated with GLUD1 and PC expression, whereas sensitivity to WH-4-023 was correlated with MAPT expression (Figure 9A). Further molecular docking analysis was performed to assess the possible interactions between these candidate compounds and their target proteins. The binding energies of Navitoclax to GLUD1 and PC were predicted to be -9.9 kcal/mol and -9.5 kcal/mol, respectively, while the binding energy of WH-4-023 to MAPT was predicted to be -8.3 kcal/mol (Figure 9B). These results indicate possible protein-ligand interactions and should be interpreted as hypothesis-generating evidence that requires further experimental validation.

Discussion

GBM remains a major clinical challenge due to marked molecular heterogeneity, frequent recurrence, and persistently poor prognosis [34–36]. The major contribution of this study is the identification of a MAPT-PC-GLUD1-defined molecular state that integrates metabolic-cellular programs, immune regulation, prognosis, and MRI-visible spatial heterogeneity. Unlike conventional prognostic signatures that primarily stratify survival, this signature provides a biologically interpretable axis linking transcriptomic alterations to tumor ecosystem features and non-invasive imaging phenotypes. In the present study, lower MAPT, PC, and GLUD1 expression defined a low-signature state associated with adverse clinicomolecular characteristics, an immunoregulatory microenvironment, and spatially heterogeneous radiomic patterns, supporting its potential relevance as an integrative marker of GBM progression.

Across bulk transcriptomic datasets, MAPT, PC, and GLUD1 were consistently downregulated in tumor tissues relative to normal brain tissues, and in extended validation analyses including glioma cohorts,

expression of all three genes generally decreased with increasing WHO grade and was associated with unfavorable clinicomolecular characteristics, including IDH wild-type and 1p/19q non-codeletion. These findings suggest that the low-signature state may reflect a more malignant and less differentiated glioma phenotype. Importantly, whereas the discovery framework was centered on GBM-focused datasets, clinicopathological validation was extended to glioma cohorts, explaining associations with grade- and subtype-related variables.

Functionally, PC and GLUD1 encode key enzymes in central carbon metabolism: PC supports anaplerosis by replenishing TCA-cycle intermediates, whereas GLUD1 links glutamine/glutamate metabolism to TCA-cycle flux via oxidative deamination [38–39]. Single-cell analyses revealed that both genes were enriched in astrocytic lineages and detectable in astrocyte-like malignant cells, suggesting that glial-like metabolic programs may contribute to heterogeneity within the low-signature axis. In contrast, MAPT encodes tau, a microtubule-stabilizing protein, predominantly expressed in neuronal populations, with limited expression in tumor cells [40–44]. Reduced MAPT expression may reflect loss of differentiated neuronal-like or cytoskeletal programs, although this remains speculative and requires functional validation. Compared with MAPT, GLUD1 and PC may have closer links to metabolic and immune context, but mechanistic underpinnings remain to be experimentally clarified [45–49].

Immune profiling revealed that tumors with lower signature-gene expression exhibited higher expression of checkpoint- and exhaustion-related genes, including CD274 (PD-L1), CTLA4, LAG3, TIGIT, CD47, ICOS, CD28, and IDO1, indicating a more immunoregulatory or exhaustion-associated transcriptional milieu. Integration of the gene signature with clinicomolecular variables enabled construction of a nomogram with acceptable calibration and potential net benefit for individualized risk stratification. Promoter methylation showed weak or no correlation with transcript abundance and was not significantly associated with OS, PFS, or DSS, whereas hub-gene expression consistently inversely correlated with TMB, suggesting that tumors with lower hub-gene expression may harbor higher mutational burden.

We designed an exploratory radiogenomic model to estimate the MAPT-PC-GLUD1 signature using MRI-based radiomic features to address spatial heterogeneity. Wavelet-transformed and gray-level run-length matrix (GLRLM) features that contributed to feature selection were found to reflect intratumoral complexity in tissue architecture, cellular density, and necrosis. Machine learning classifiers, especially Random Forest and XGBoost, showed moderate to good performance, and decision curve analysis showed that they could be useful within certain threshold ranges. However, voxel-wise maps are imaging-based surrogates rather than direct spatial measures of gene expression and should be interpreted as hypothesis-generating.

Lastly, pharmacogenomic screening and in silico docking revealed candidate compounds related to the MAPT-PC-GLUD1 signature. Navitoclax and WH-4-023 showed good correlations in GDSC assays, and docking indicated favorable binding affinities with PC/GLUD1 and MAPT, respectively [50-53]. These findings provide a rationale for further investigation but remain exploratory; their activities may be either direct or indirect, through broader alterations of metabolic, cytoskeletal, and biosynthetic programs.

There are several limitations to be considered. To begin with, the analyses were mostly retrospective and population-based and need to be validated in independent prospective cohorts and experimental systems. Second, despite the promising internal predictive performance of the radiomic models, multicenter prospective cohorts with standardized MRI acquisition are required to assess their robustness and generalizability. Third, it is not possible to infer causal relationships between the MAPT-PC-GLUD1 signature and metabolic, biosynthetic, immune, or imaging-derived states. Fourth, the incremental prognostic value of this signature compared with current GBM metabolic, immune, or radiogenomic signatures was not tested. Lastly, since the clinicopathological validation used glioma cohorts, not all of the associations may be specific to GBM but may instead reflect glioma biology more broadly. To establish the role of this signature in GBM evolution and drug resistance, functional perturbation experiments, metabolic flux assays, spatial transcriptomics, and external radiogenomic validation are required.

Abbreviations

Abbreviation	Definition
AUC	Area under the receiver operating characteristic curve
CDF	Cumulative distribution function
CGGA	Chinese Glioma Genome Atlas
CI	Confidence interval
CNS	Central nervous system
DCA	Decision curve analysis
DEG	Differentially expressed gene
DECG	Differentially expressed candidate gene
DSS	Disease-specific survival
FDR	False discovery rate
GBM	Glioblastoma
GDC	Genomic Data Commons
GDSC	Genomics of Drug Sensitivity in Cancer
GEO	Gene Expression Omnibus
GLCM	Gray-level co-occurrence matrix
GLDM	Gray-level dependence matrix
GLRLM	Gray-level run-length matrix
GLSZM	Gray-level size zone matrix
GLUD1	Glutamate dehydrogenase 1
GO	Gene Ontology
GSEA	Gene set enrichment analysis
GSVA	Gene set variation analysis
HR	Hazard ratio
IC50	Half-maximal inhibitory concentration
ICB	Immune checkpoint blockade
IDH	Isocitrate dehydrogenase
KEGG	Kyoto Encyclopedia of Genes and Genomes
KNN	K-nearest neighbor

Abbreviation	Definition
LASSO	Least absolute shrinkage and selection operator
LoG	Laplacian of Gaussian
MAPT	Microtubule-associated protein tau
MGMT	O6-methylguanine-DNA methyltransferase
MLP	Multilayer perceptron
MRI	Magnetic resonance imaging
MSI	Microsatellite instability
NES	Normalized enrichment score
NK	Natural killer
OPCs	Oligodendrocyte precursor cells
OS	Overall survival
PC	Pyruvate carboxylase
PCA	Principal component analysis
PDB	Protein Data Bank
PD-1	Programmed cell death protein 1
PD-L1	Programmed death-ligand 1
PFI	Progression-free interval
PFS	Progression-free survival
RF	Random Forest
RiBi	Ribosome biogenesis
ROC	Receiver operating characteristic
ROI	Region of interest
scRNA-seq	Single-cell RNA sequencing
SVM-RFE	Support vector machine-recursive feature elimination
T1CE	Contrast-enhanced T1-weighted imaging
TCGA	The Cancer Genome Atlas
TCA	Tricarboxylic acid
TIDE	Tumor Immune Dysfunction and Exclusion

Abbreviation	Definition
TMB	Tumor mutational burden
TME	Tumor microenvironment
TPM	Transcripts per million
Tregs	Regulatory T cells
t-SNE	t-distributed stochastic neighbor embedding
WGCNA	Weighted gene co-expression network analysis
WHO	World Health Organization
XGBoost	Extreme gradient boosting

Declarations

Acknowledgments

The authors give credit to the public databases TCGA , CGGA, and GEO for providing the datasets analyzed in this study. The authors declare no conflicts of interest.

The Data Availability statement

All datasets and public resources analyzed in this study are publicly available. GEO datasets were obtained from the NCBI Gene Expression Omnibus under accession numbers GSE4290, GSE116520, and GSE84465. RNA-seq expression profiles, clinicopathological data, MSI, TMB, and mutation-related information for GBM patients were retrieved from the TCGA-GBM project via the Genomic Data Commons (GDC) Data Portal. No additional somatic mutation calling was performed. Corresponding MRI data were obtained from The Cancer Imaging Archive (TCIA), specifically the TCGA-GBM imaging collection. CGGA transcriptomic and clinical data were retrieved from the mRNAseq_325 and mRNAseq_693 cohorts, and CGGA MRI data were obtained from the Image-genomic data dataset, which contains 268 MRI-based image-genomic samples. After matching transcriptomic, clinicopathological, and preoperative contrast-enhanced T1-weighted MRI data from TCGA/TCIA and CGGA, 92 GBM patients were included in the final radiogenomic analysis.

Metabolism- and ribosome biogenesis-related genes were obtained from GeneCards, and enrichment analyses were performed using MSigDB v2023.2 C2 curated gene sets. Drug sensitivity data were obtained from GDSC2 on June 1, 2025. Single-cell RNA-seq data were accessed through TISCH/TISCH2 using the dataset corresponding to GSE84465. Promoter methylation analyses were performed using UALCAN based on TCGA data. Protein structures for molecular docking were retrieved from the Protein Data Bank (PDB), including GLUD1 (8SK8), PC (3BG3), and MAPT (4FL5). No new datasets were

generated in this study. Processed data and analysis scripts are available from the corresponding author upon reasonable request.

Funding

This research received no external funding.

Ethics declarations

Competing interests

The authors declare no competing interests.

Ethics, Consent to Participate, and Consent to Publish declarations

This study did not involve human participants or animal subjects; therefore, ethical approval and consent to participate were not required.

Author contributions

Y-XH conceived and designed the study, developed the methodology, gathered and analyzed the data, coordinated the project, and drafted and revised the manuscript.

W-Z gathered and analyzed the data, coordinated the project, and drafted and revised the manuscript.

L-CC gathered and analyzed the data, coordinated the project, and drafted and revised the manuscript.

Q-DH gathered and analyzed the data, coordinated the project, and drafted and revised the manuscript.

Z-YT gathered and analyzed the data, coordinated the project, and drafted and revised the manuscript.

L-J assisted in the study design, data processing, analysis, and methodological implementation and provided supervision, visualization, and critical revision of the manuscript.

References

1. Louis DN, et al. The 2021 WHO Classification of Tumors of the Central Nervous System: a summary. Neuro-oncology vol. 2021;23:1231–51. 10.1093/neuonc/noab106.
2. Wen PY, Reardon DA. Neuro-oncology in 2015: Progress in glioma diagnosis, classification and treatment. Nat reviews Neurol vol. 2016;12(2):69–70. 10.1038/nrneurol.2015.242.
3. Karimi E, et al. Single-cell spatial immune landscapes of primary and metastatic brain tumours. Nat vol. 2023;614:555–63. 10.1038/s41586-022-05680-3.
4. Jayaram M, Anjali, Joanna JP. Role of the Microenvironment in Glioma Pathogenesis. Annu Rev Pathol. 2024;19:181–201. 10.1146/annurev-pathmechdis-051122-110348.

5. Stupp R, et al. Radiotherapy plus concomitant and adjuvant temozolomide for glioblastoma. New Engl J Med vol. 2005;352:987–96. 10.1056/NEJMoa043330.
6. Weller M et al. Jan. Improved prognostic stratification of patients with isocitrate dehydrogenase-mutant astrocytoma. Acta neuropathologica vol. 147,1 11. 6 2024, 10.1007/s00401-023-02662-1
7. Zhang R et al. RNA-Seq Reveals the Mechanism of Synergistic Hydrogen-Chemotherapy Based on Active Magnesium Micromotors for Inhibiting Glioblastoma Recurrence by Modulating Tumor Microenvironment. Small vol. 21,20 (2025): e2408809. 10.1002/smll.202408809
8. Liu Z et al. Sep. Single-cell analysis of 5-aminolevulinic acid intraoperative labeling specificity for glioblastoma. Journal of neurosurgery vol. 140,4 968–978. 22 2023, 10.3171/2023.7. JNS 23122.
9. Zhang L, et al. SIRT3 and SIRT4 double-genes remodeled the mitochondrial network to induce hepatocellular carcinoma cell line differentiation and suppress malignant phenotypes. Biochem Pharmacol. 2024;223:116168. 10.1016/j.bcp. 2024.116168.
10. Yang R et al. Apr. POU2F2 regulates glycolytic reprogramming and glioblastoma progression via PDPK1-dependent activation of PI3K/AKT/mTOR pathway. Cell death & disease vol. 12,5 433. 30 2021, 10.1038/s41419-021-03719-3
11. Yang R, et al. Glutamate dehydrogenase 1-catalytic glutaminolysis feedback activates EGFR/PI3K/AKT pathway and reprograms glioblastoma metabolism. Neuro-oncology vol. 2025;27(3):668–81. 10.1093/neuonc/noae222.
12. Liu S, et al. LncRNAs-circRNAs as Rising Epigenetic Binary Superstars in Regulating Lipid Metabolic Reprogramming of Cancers. Adv Sci vol. 2024;11(1):e2303570. 10.1002/advs.202303570.
13. Bezawork-Geleta A, et al. Metabolic Plasticity of Glioblastoma Cells in Response to DHODH Inhibitor BAY2402234 Treatment. Metabolites 14,8 413. 27 Jul. 2024. 10.3390/metabo14080413.
14. Galloway A, et al. Upregulation of RNA cap methyltransferase RNMT drives ribosome biogenesis during T cell activation. Nucleic acids Res vol. 2021;49:6722–38. 10.1093/nar/gkab465.
15. Cao Y et al. Nov. UCHL5 Promotes Proliferation and Migration of Bladder Cancer Cells by Activating c-Myc via AKT/mTOR Signaling. Cancers vol. 14,22 5538. 10 2022, 10.3390/cancers14225538
16. Zhou L et al. Oct. Metabolic Reprogramming of Cancer-Associated Fibroblast in the Tumor Microenvironment: From Basics to Clinic. Clinical Medicine Insights. Oncology vol. 18 11795549241287058. 21 2024, 10.1177/11795549241287058
17. Gan Y, et al. UTP11 deficiency suppresses cancer development via nucleolar stress and ferroptosis. Redox Biol. 2023;62:102705. 10.1016/j.redox.2023.102705.
18. Cao Y, et al. Activation of γ2-AMPK Suppresses Ribosome Biogenesis and Protects Against Myocardial Ischemia/Reperfusion Injury. Circulation Res vol. 2017;121:1182–91. 10.1161/CIRCRESAHA.117.311159.
19. Hoxhaj G, et al. The mTORC1 Signaling Network Senses Changes in Cellular Purine Nucleotide Levels. Cell Rep vol. 2017;21(5):1331–46. 10.1016/j.celrep.2017.10.029.

20. Claiborne MD et al. Persistent CAD activity in memory $CD8^+$ T cells supports rRNA synthesis and ribosomal biogenesis required at rechallenge. Sci Immunol vol 7,71 (2022): eabh4271. 10.1126/sciimmunol.abh4271
21. Ji X, et al. Mitochondrial ribosomal protein L12 potentiates hepatocellular carcinoma by regulating mitochondrial biogenesis and metabolic reprogramming. Metab Clin Exp. 2024;152:155761. 10.1016/j.metabol.2023.155761.
22. Miki K et al. Nov. Glutaminolysis is associated with mitochondrial pathway activation and can be therapeutically targeted in glioblastoma. Cancer & metabolism vol. 12,1 35. 19 2024, 10.1186/s40170-024-00364-0
23. Paraqindes H, et al. Isocitrate dehydrogenase wt and IDHmut adult-type diffuse gliomas display distinct alterations in ribosome biogenesis and 2'O-methylation of ribosomal RNA. Neuro-oncology vol. 2023;25(12):2191–206. 10.1093/neuonc/noad140.
24. Zisi A, et al. Small molecule-mediated disruption of ribosome biogenesis synergizes with FGFR inhibitors to suppress glioma cell growth. Neuro-oncology vol. 2023;25(6):1058–72. 10.1093/neuonc/noac286.
25. Yang K et al. The role of lipid metabolic reprogramming in tumor microenvironment. Theranostics 13,6 1774–808. 13 Mar. 2023, 10.7150/thno.82920
26. Reuter G, et al. Conventional and advanced imaging throughout the cycle of care of gliomas. Neurosurgical Rev vol. 2021;44(5):2493–509. 10.1007/s10143-020-01448-3.
27. Gatto L et al. Dec. Beyond Imaging and Genetic Signature in Glioblastoma: Radiogenomic Holistic Approach in Neuro-Oncology. Biomedicines vol. 10,12 3205. 9 2022, 10.3390/biomedicines10123205
28. Beig N, et al. Introduction to radiomics and radiogenomics in neuro-oncology: implications and challenges. Neuro-oncology advances 2,Suppl 4 iv3-iv14. 23 Jan. 2021. 10.1093/noajnl/vdaa148.
29. Lasocki A, et al. Conventional MRI features of adult diffuse glioma molecular subtypes: a systematic review. Neuroradiol vol. 2021;63(3):353–62. 10.1007/s00234-020-02532-7.
30. Samartha MV et al. Sai Jan. AI-driven estimation of O6 methylguanine-DNA-methyltransferase (MGMT) promoter methylation in glioblastoma patients: a systematic review with bias analysis. Journal of cancer research and clinical oncology vol. 150,2 57. 31 2024, 10.1007/s00432-023-05566-5
31. Singh G et al. Oct. -New frontiers in domain-inspired radiomics and radiogenomics: increasing role of molecular diagnostics in CNS tumor classification and grading following WHO CNS-5 updates. Cancer imaging: the official publication of the International Cancer Imaging Society vol. 24,1 133. 7 2024, 10.1186/s40644-024-00769-6
32. Davalan W, Alkins R. Prognostic and predictive determinants in high-grade gliomas: integrating tumor-intrinsic biology with patient and system-level factors. Frontiers in neurology vol. 16 1664458. 19 Nov. 2025, 10.3389/fneur.2025.1664458

33. Buzdugan S et al. Oct. Radiogenomics for Glioblastoma Survival Prediction: Integrating Radiomics, Clinical, and Genomic Features Using Artificial Intelligence. Journal of imaging informatics in medicine. 10.1007/s10278-025-01692-3. 8 2025, doi:10.1007/s10278-025-01692-3.
34. Sanai N. Integrated genomic analysis identifies clinically relevant subtypes of glioblastoma. World Neurosurg vol. 2010;74(1):4–5. 10.1016/j.wneu.2010.08.011.
35. Patel AP et al. Single-cell RNA-seq highlights intratumoral heterogeneity in primary glioblastoma. Science 344,6190 (2014): 1396–401. 10.1126/science.1254257
36. Furtak J, et al. Survival after reoperation for recurrent glioblastoma multiforme: A prospective study. Surg Oncol. 2022;42:101771. 10.1016/j.suronc.2022.101771.
37. Bruno G, et al. TRAP1 regulates the response of colorectal cancer cells to hypoxia and inhibits ribosome biogenesis under conditions of oxygen deprivation. Int J Oncol vol. 2022;60(6):79. 10.3892/ijo.2022.5369.
38. Renoult Ophélie, et al. Metabolic profiling of glioblastoma stem cells reveals pyruvate carboxylase as a critical survival factor and potential therapeutic target. Neuro-oncology vol. 2024;26(9):1572–86. 10.1093/neuonc/noae106.
39. Yang C, et al. Glioblastoma cells require glutamate dehydrogenase to survive impairments of glucose metabolism or Akt signaling. Cancer Res vol. 2009;69:7986–93. 10.1158/0008-5472. CAN-09-2266.
40. Weingarten MD et al. A protein factor essential for microtubule assembly. Proceedings of the National Academy of Sciences of the United States of America 72,5 (1975): 1858–62. 10.1073/pnas.72.5.1858
41. Pagano A et al. Nov. Tau Regulates Glioblastoma Progression, 3D Cell Organization, Growth and Migration via the PI3K-AKT Axis. Cancers vol. 13,22 5818. 19 2021, 10.3390/cancers13225818
42. Schroeder C et al. Mar. Aberrant expression of the microtubule-associated protein tau is an independent prognostic feature in prostate cancer. BMC cancer vol. 19,1 193. 1 2019, 10.1186/s12885-019-5390-1
43. Sekino Y et al. Microtubule-associated protein tau (MAPT) promotes bicalutamide resistance and is associated with survival in prostate cancer. Urologic oncology vol. 38,10 (2020): 795.e1-795.e8. 10.1016/j.urolonc.2020.04.032
44. Liu X, et al. Accumulation of microtubule-associated protein tau promotes hepatocellular carcinogenesis through inhibiting autophagosome-lysosome fusion. Mol Cell Biochem vol. 2025;480:3621–35. 10.1007/s11010-024-05193-9.
45. Frigerio F et al. Deletion of glutamate dehydrogenase 1 (Glud1) in the central nervous system affects glutamate handling without altering synaptic transmission. J Neurochem 123,3 (2012): 342–8. 10.1111/j.1471-4159.2012.07933.x
46. Bao X et al. Transgenic expression of Glud1 (glutamate dehydrogenase 1) in neurons: in vivo model of enhanced glutamate release, altered synaptic plasticity, and selective neuronal vulnerability. J neuroscience: official J Soc Neurosci 29,44 (2009): 13929–44. 10.1523/JNEUROSCI.4413-09.2009

47. Wang Q, et al. Therapeutic targeting of glutamate dehydrogenase 1 that links metabolic reprogramming and Snail-mediated epithelial-mesenchymal transition in drug-resistant lung cancer. Pharmacol Res. 2022;185:106490. 10.1016/j.phrs.2022.106490.
48. Liu S. Bioinformatics analysis identifies GLUD1 as a prognostic indicator for clear cell renal cell carcinoma. European journal of medical research vol. 29,1 70. 20 Jan. 2024, 10.1186/s40001-024-01649-2
49. Renoult Ophélie, et al. Metabolic profiling of glioblastoma stem cells reveals pyruvate carboxylase as a critical survival factor and potential therapeutic target. Neuro-oncology vol. 2024;26(9):1572–86. 10.1093/neuonc/noae106.
50. Stamelos VA, et al. Navitoclax augments the activity of carboplatin and paclitaxel combinations in ovarian cancer cells. Gynecologic Oncol vol. 2013;128(2):377–82. 10.1016/j.ygyno.2012.11.019.
51. Lee EY et al. Human breast cancer cells display different sensitivities to ABT-263 based on the level of survivin. Toxicology in vitro: an international journal published in association with BIBRA 46 (2018): 229–36. 10.1016/j.tiv.2017.09.023
52. Wang X et al. Dec. Development and validation of a cuproptosis-related lncRNA model correlated to the cancer-associated fibroblasts enable the prediction prognosis of patients with osteosarcoma. Journal of bone oncology vol. 38 100463. 9 2022, 10.1016/j.jbo.2022.100463
53. Guo A et al. Sep. Prognosis and immunotherapeutic implications of molecular classification of cervical cancer based on immunophenoscore-related genes. Journal of biomolecular structure & dynamics, 1–16. 23 2024, 10.1080/07391102.2024.2404545

Figures

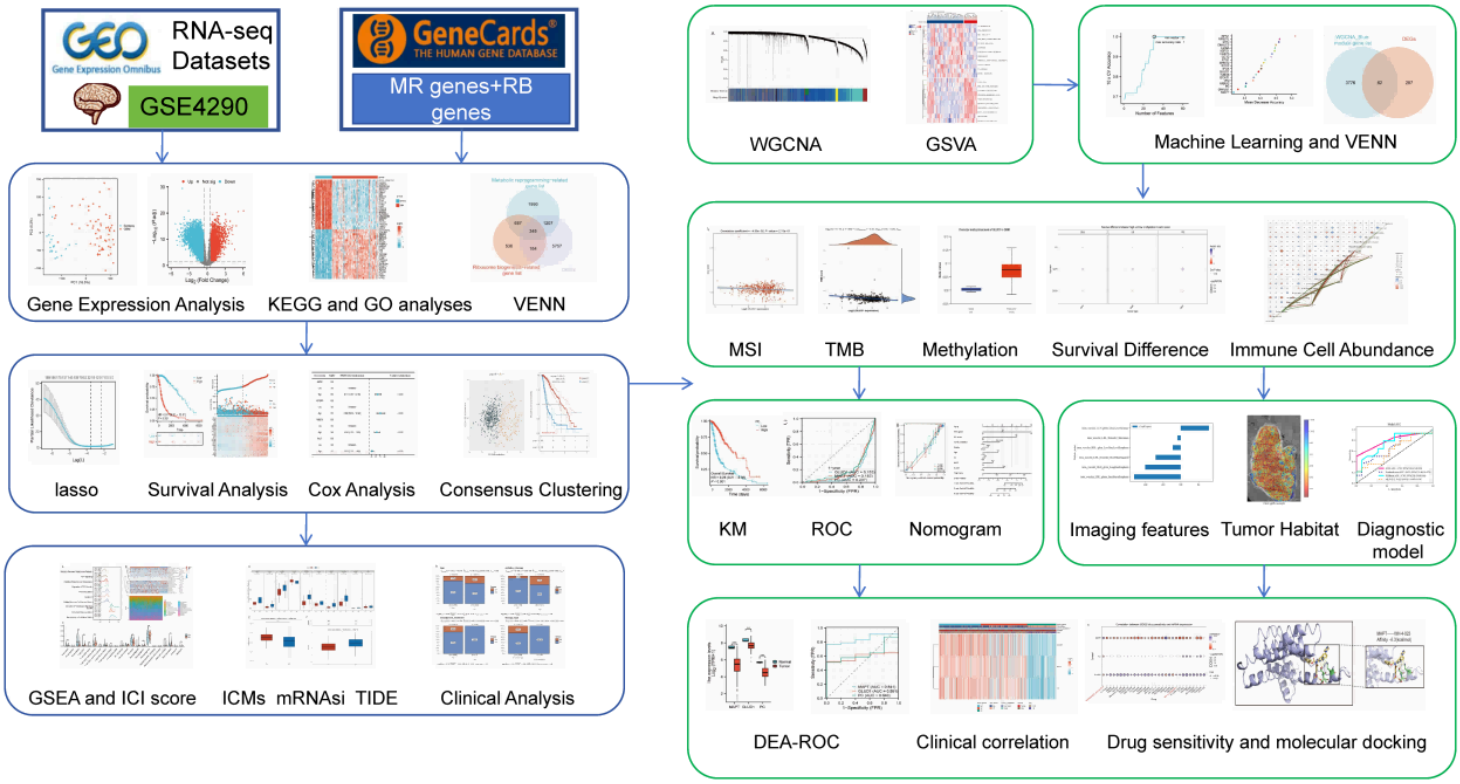


Figure 1

The flowchart of the study.

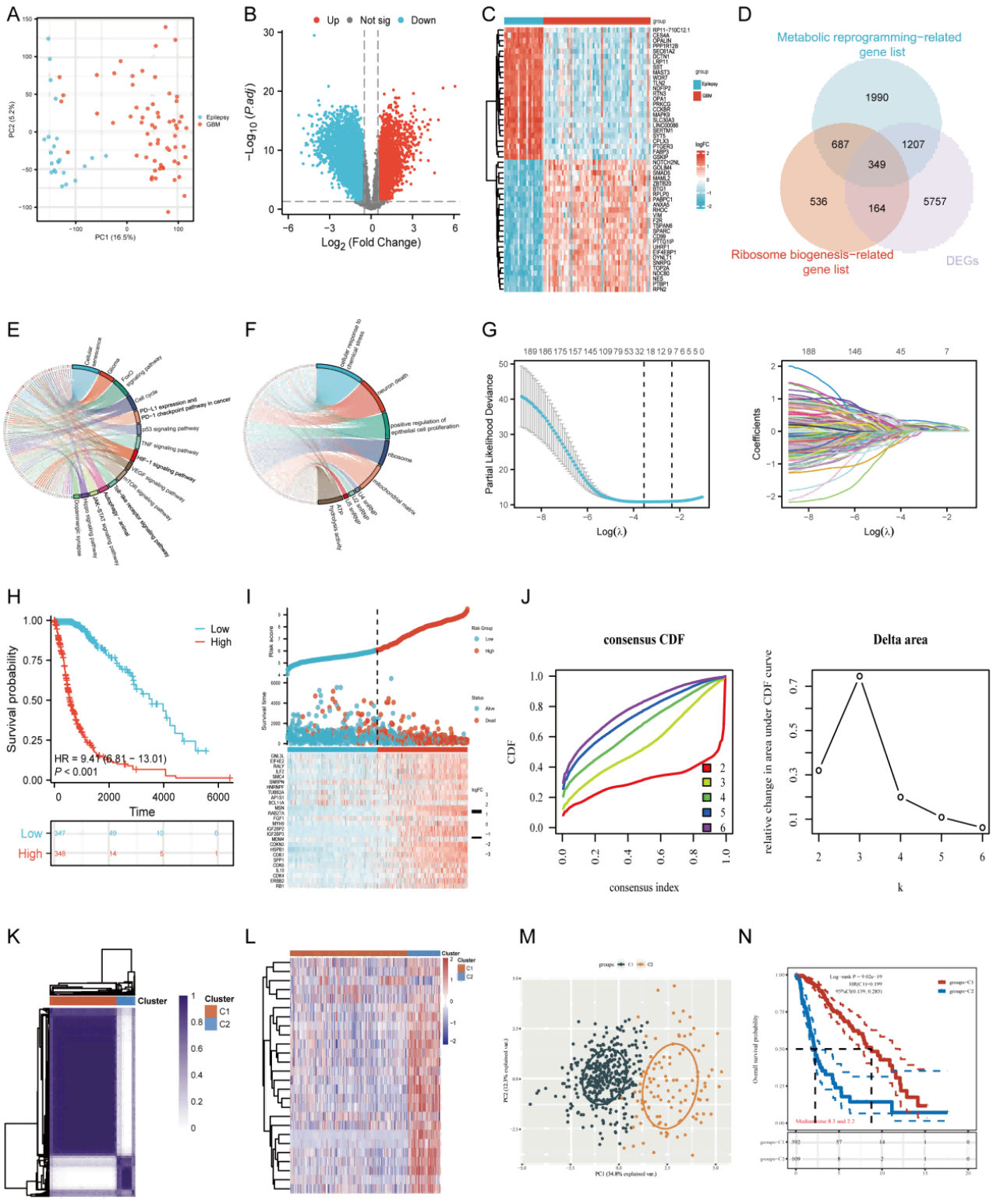


Figure 2

Identification and functional characterization of metabolism- and ribosome biogenesis–related differentially expressed genes in GBM.

(A) PCA of the GSE4290 cohort showing distinct transcriptional separation between GBM tissues (red) and non-tumor brain samples (turquoise).

(B) Volcano plot of DEGs between GBM and control samples ($|\log_2 FC| > 0.5$, FDR < 0.05). Upregulated genes are shown in red, downregulated genes in turquoise, and non-significant genes in grey.

(C) Heatmap of representative DEGs demonstrating distinct expression patterns between tumor and normal tissues.

(D) Venn diagram illustrating the overlap among DEGs (n = 5,757), metabolism-related genes, and ribosome biogenesis–related genes, identifying 349 candidate genes associated with a metabolic–ribosomal transcriptional program.

(E) KEGG pathway enrichment analysis showing that these genes are enriched in pathways related to cell cycle regulation, apoptosis, glioma signaling, and immune-related pathways, including PD-1/PD-L1 signaling.

(F) GO biological process analysis indicating enrichment in oxidative stress response, cell proliferation, ribosome biogenesis, and mitochondrial function.

(G) Ten-fold cross-validation curve of the LASSO Cox regression model based on 349 DECGs, showing the optimal λ values and the corresponding numbers of non-zero genes. LASSO coefficient profiles of the DECGs across log(λ), with the selected λ yielding a 25-gene prognostic signature.

(H) Kaplan-Meier overall survival (OS) curves for the high- and low-risk groups stratified by the median risk score derived from the 25-gene signature in the TCGA cohort. Patients in the high-risk group exhibited significantly worse OS than those in the low-risk group (HR ≈ 9.4, 95% CI 6.81-13.01, $P < 0.001$).

(I) Distribution of risk scores (top), survival status (middle), and heatmap of the 25-gene expression pattern (bottom), with samples ordered by increasing risk score. Turquoise indicates low risk/alive and red indicates high risk/dead; in the heatmap, red denotes high expression and turquoise denotes low expression.

(J) Cumulative distribution function (CDF) curves of consensus scores for cluster numbers k = 2-6, illustrating clustering stability across different values of k.

(K) Relative change in the area under the CDF curve (delta area) for k = 2-6. The inflection point indicated that k = 2 was the optimal number of clusters.

(L) Consensus clustering matrix heatmap for k = 2, identifying two stable molecular subtypes: C1 and C2.

(M) PCA plot showing the spatial distribution of the two molecular subtypes. The two clusters were clearly separated based on the first two principal components (PC1: 34.8%; PC2: 12.3%), with C1 shown in blue and C2 in red.

(N) Kaplan-Meier OS curves comparing the two molecular subtypes, showing that patients in C1 had significantly longer OS than those in C2 (log-rank $P = 9.02 \times 10^{-19}$; HR for C1 = 0.199, 95% CI 0.139-0.285).

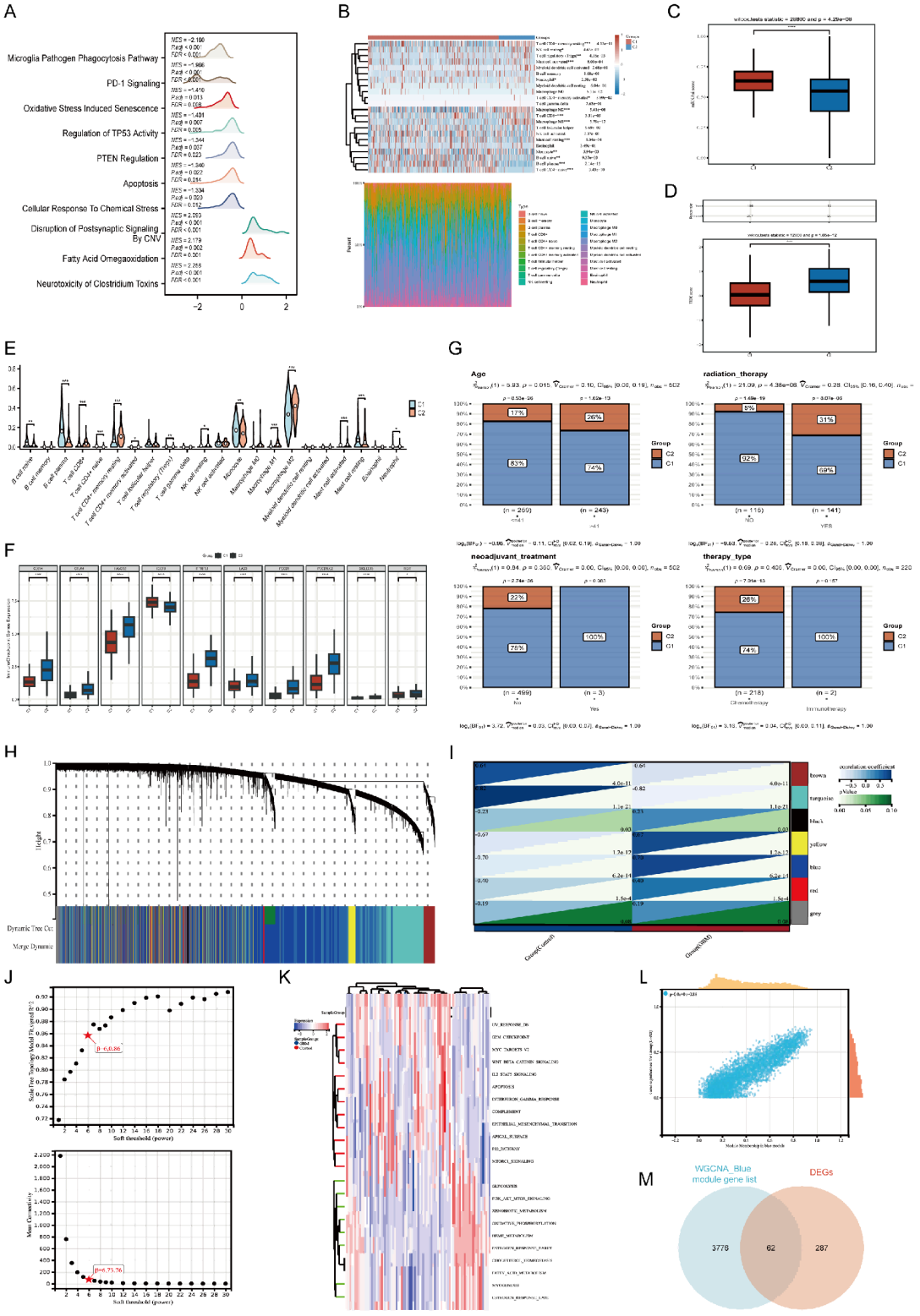


Figure 3

Immune landscape and clinical characteristics of GBM molecular subtypes, and identification of core co-expression modules and genes based on WGCNA and GSVA.

(A) GSEA showing the differentially enriched pathways between the prognostically favorable C1 subtype and the poor-prognosis C2 subtype.

(B) Heatmap showing the relative abundance of 22 tumor-infiltrating immune cell types across molecular subtypes (C1 vs. C2), accompanied by stacked bar plots representing immune cell composition in individual samples.

(C) Comparison of mRNA-based stemness signatures between C1 and C2, showing that the C2 subtype exhibited significantly higher stemness features.

(D) Predicted response to immune checkpoint blockade (ICB) therapy and TIDE scores across molecular subtypes, showing a higher proportion of non-responders and elevated TIDE scores in the C2 subtype.

(E) Violin plots showing significant differences in immune cell infiltration between C1 and C2 ($P < 0.05$, $*P < 0.01$, $**P < 0.001$, $***P < 0.0001$).

(F) Boxplots of immune checkpoint gene expression, indicating that most inhibitory immune checkpoint molecules were expressed at higher levels in the C2 subtype.

(G) Stacked bar plots showing the associations between molecular subtypes (C1 in blue, C2 in red) and clinical characteristics, including age, radiotherapy, neoadjuvant therapy, and systemic treatment type.

(H) WGCNA cluster dendrogram based on the GSE4290 dataset, with color annotations indicating gene modules identified before and after dynamic tree cutting and module merging.

(I) Module-trait relationship heatmap showing correlations between module eigengenes and phenotypes (GBM vs. control). The blue module exhibited the strongest positive correlation with GBM and a negative correlation with normal tissue.

(J) Network topology analysis used to determine the soft-thresholding power, showing the scale-free topology fit index (upper panel) and mean connectivity (lower panel). The optimal soft threshold was set at $\beta = 6$ ($R^2 \approx 0.86$).

(K) GSVA heatmap showing the enrichment of representative Hallmark pathways and metabolism-related pathways in GBM and control samples (top annotation: red = GBM, blue = control).

(L) Scatter plot showing a strong positive correlation between module membership and gene significance within the blue module ($r = 0.88$, $P < 0.001$).

(M) Venn diagram showing the overlap between blue module genes (n = 3,776) and differentially expressed genes (DEGs, n = 349), identifying 62 hub genes for subsequent analyses.

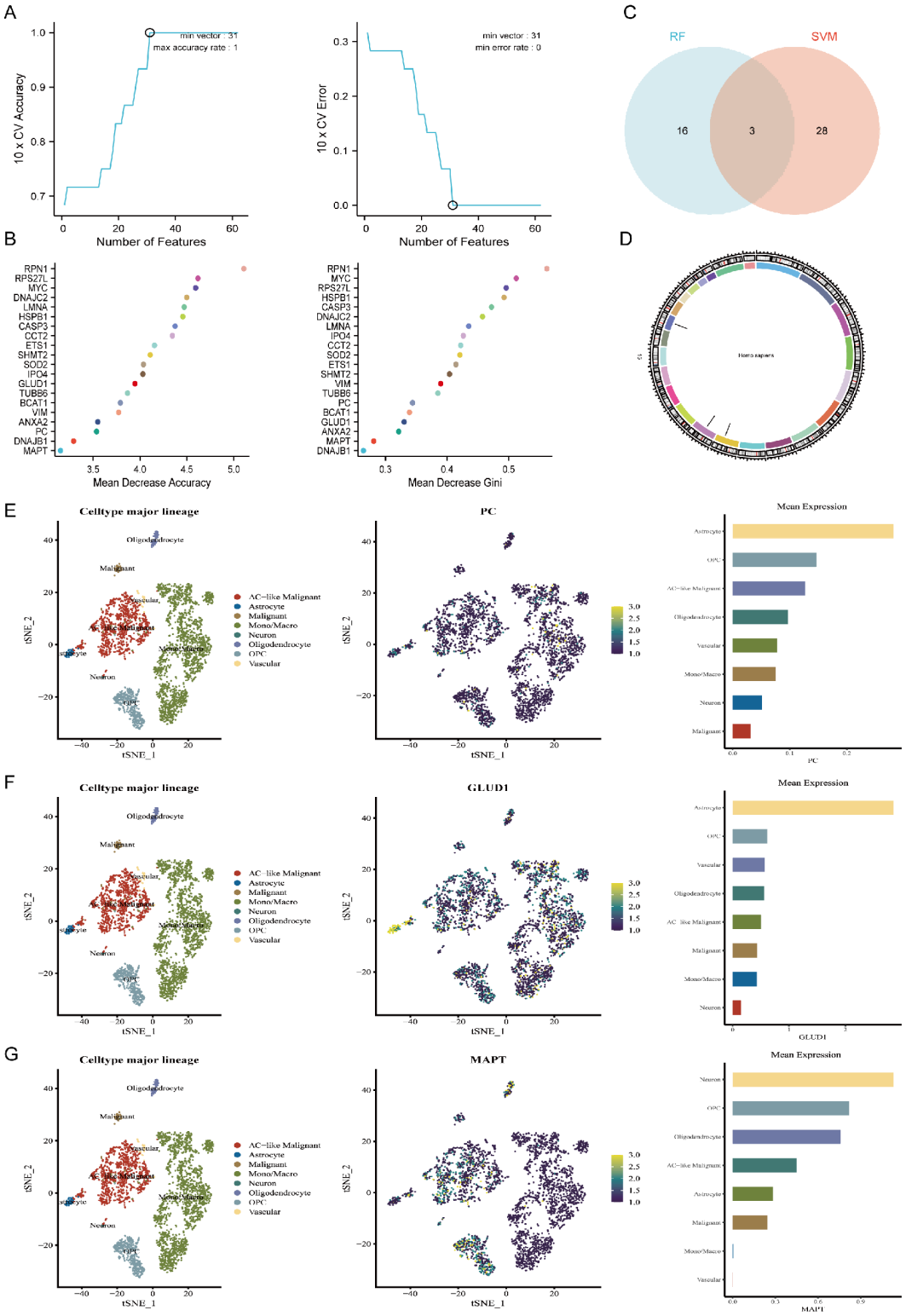


Figure 4

Identification of the MAPT-PC-GLUD1 Signature Based on Machine Learning, Genomic Distribution, and Single-Cell Expression Patterns in the Microenvironment.

(A) Ten-fold cross-validation accuracy curve of the SVM-RFE classifier constructed from 62 candidate hub genes, showing that the optimal subset of 31 genes achieved the highest classification accuracy of

1.0.

(B) Random Forest variable importance plot showing the mean decrease in accuracy (left) and mean decrease in Gini index (right) for the candidate genes.

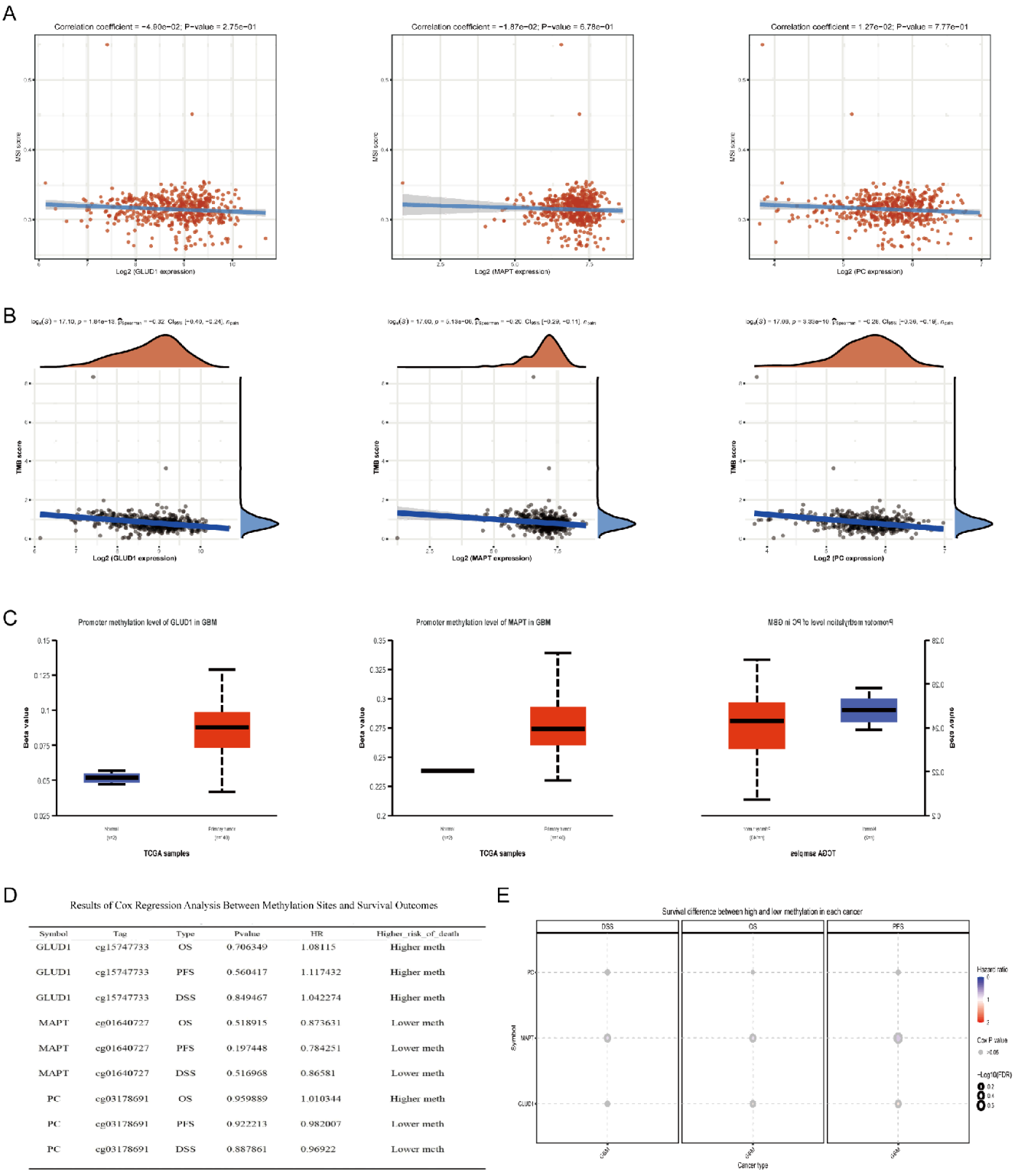
(C) Venn diagram showing the overlap between genes identified by Random Forest (turquoise) and SVM-RFE (pink), highlighting three shared genes retained in the MAPT-PC-GLUD1 signature: GLUD1, PC, and MAPT.

(D) Circos plot showing the chromosomal locations of the three genes: GLUD1 at 10q23.2, PC at 11q13.2, and MAPT at 17q21.31.

(E) t-SNE plot of single-cell RNA sequencing (scRNA-seq) data from the glioma dataset in the TISCH database, colored by major cell lineages, together with the feature plot of GLUD1 expression and a bar plot of its average expression across cell lineages. GLUD1 was most highly expressed in astrocytes, with moderate expression in oligodendrocyte precursor cells (OPCs), vascular cells, oligodendrocytes, and astrocyte-like (AC-like) malignant cells.

(F) Single-cell feature plot and bar plot of average expression levels for MAPT. MAPT expression was highest in neurons and was also enriched in OPCs and oligodendrocyte subpopulations, whereas its expression was relatively low in malignant cells.

(G) Distribution of PC expression across cell lineages in the glioma microenvironment. Average PC expression was highest in astrocytes and OPCs, followed by AC-like malignant cells, oligodendrocytes, vascular cells, and monocytes/macrophages, while remaining relatively low in neurons and general malignant cells.



Symbol	Tag	Type	Pvalue	HR	Higher_risk_of_death
GLUD1	cg15747733	OS	0.706349	1.08115	Higher meth
GLUD1	cg15747733	PFS	0.560417	1.117432	Higher meth
GLUD1	cg15747733	DSS	0.849467	1.042274	Higher meth
MAPT	cg01640727	OS	0.518915	0.873631	Lower meth
MAPT	cg01640727	PFS	0.197448	0.784251	Lower meth
MAPT	cg01640727	DSS	0.516968	0.86581	Lower meth
PC	cg03178691	OS	0.959889	1.010344	Higher meth
PC	cg03178691	PFS	0.922213	0.982007	Lower meth
PC	cg03178691	DSS	0.887861	0.96922	Lower meth

Figure 5

Association of GLUD1, MAPT, and PC with MSI, TMB, and promoter methylation in GBM.

(A) Spearman correlation analyses between log2-transformed expression levels of GLUD1, MAPT, and PC and MSI scores in the TCGA-GBM cohort. Each dot represents one tumor sample, and the blue line indicates the fitted regression with 95% confidence intervals.

(B) Spearman correlation analyses between log2-transformed expression levels of GLUD1, MAPT, and PC and TMB in the TCGA-GBM cohort. Density plots show the distribution of TMB values, and the blue fitted lines indicate an overall negative association between gene expression and TMB.

(C) Promoter methylation β values of GLUD1, MAPT, and PC in normal brain tissues (blue, n = 2) and primary GBM tissues (red, n ≈ 140) obtained from the TCGA dataset through the UALCAN platform.

(D) Cox regression analysis of promoter methylation at CpG sites cg15747733 (GLUD1), cg01640727 (MAPT), and cg03178691 (PC) in relation to overall survival (OS), progression-free survival (PFS), and disease-specific survival (DSS) in GBM, showing the corresponding P values, hazard ratios (HRs), and directions of risk.

(E) Bubble plot summarizing the prognostic impact of high versus low promoter methylation levels of GLUD1, MAPT, and PC on OS, DSS, and PFS. Bubble color represents HR (blue, HR < 1; red, HR > 1), and bubble size represents $-\log_{10}$(FDR).

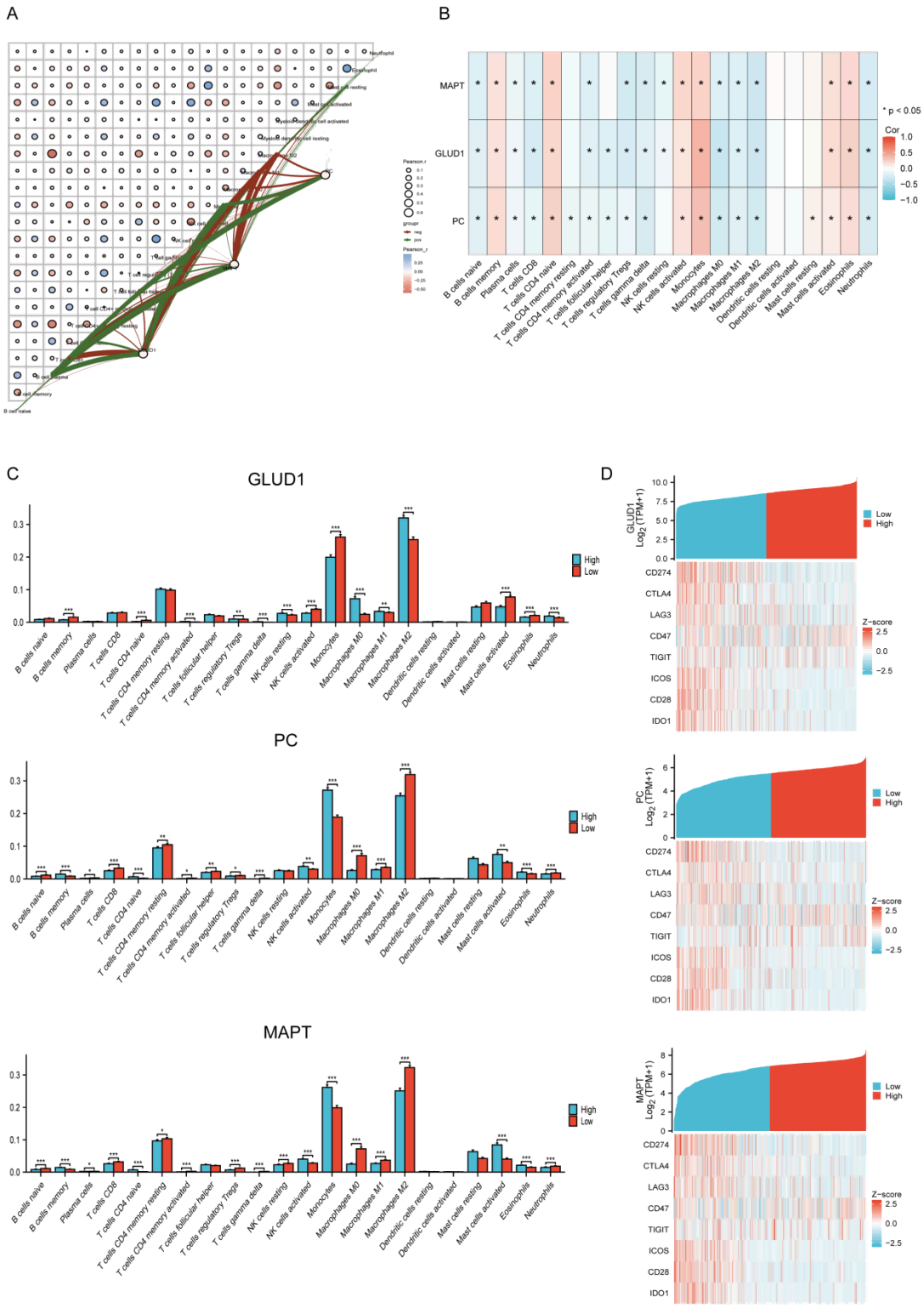


Figure 6

Genomic instability and epigenetic features related to GLUD1, PC, and MAPT in TCGA-GBM.

(A) Interaction network analysis illustrating potential cellular communication among different cell types within the tumor microenvironment.

(B) Correlation heatmap showing the relationships between the expression levels of GLUD1, MAPT, and PC and the relative abundance of 22 tumor-infiltrating immune cell types. Color gradients from blue to red indicate negative to positive correlations ($P < 0.05$).

(C) Bar plots comparing the infiltration levels of 22 immune cell types between high- and low-expression groups of GLUD1 (top), MAPT (middle), and PC (bottom). Statistical significance was assessed using the Wilcoxon rank-sum test ($P < 0.05$).

(D) Association analysis between the expression of the three hub genes and key immune checkpoint molecules (e.g., CD274, CTLA4, LAG3). The upper panels show gene expression distributions, and the lower panels present heatmaps of immune checkpoint expression profiles ranked by hub gene expression.

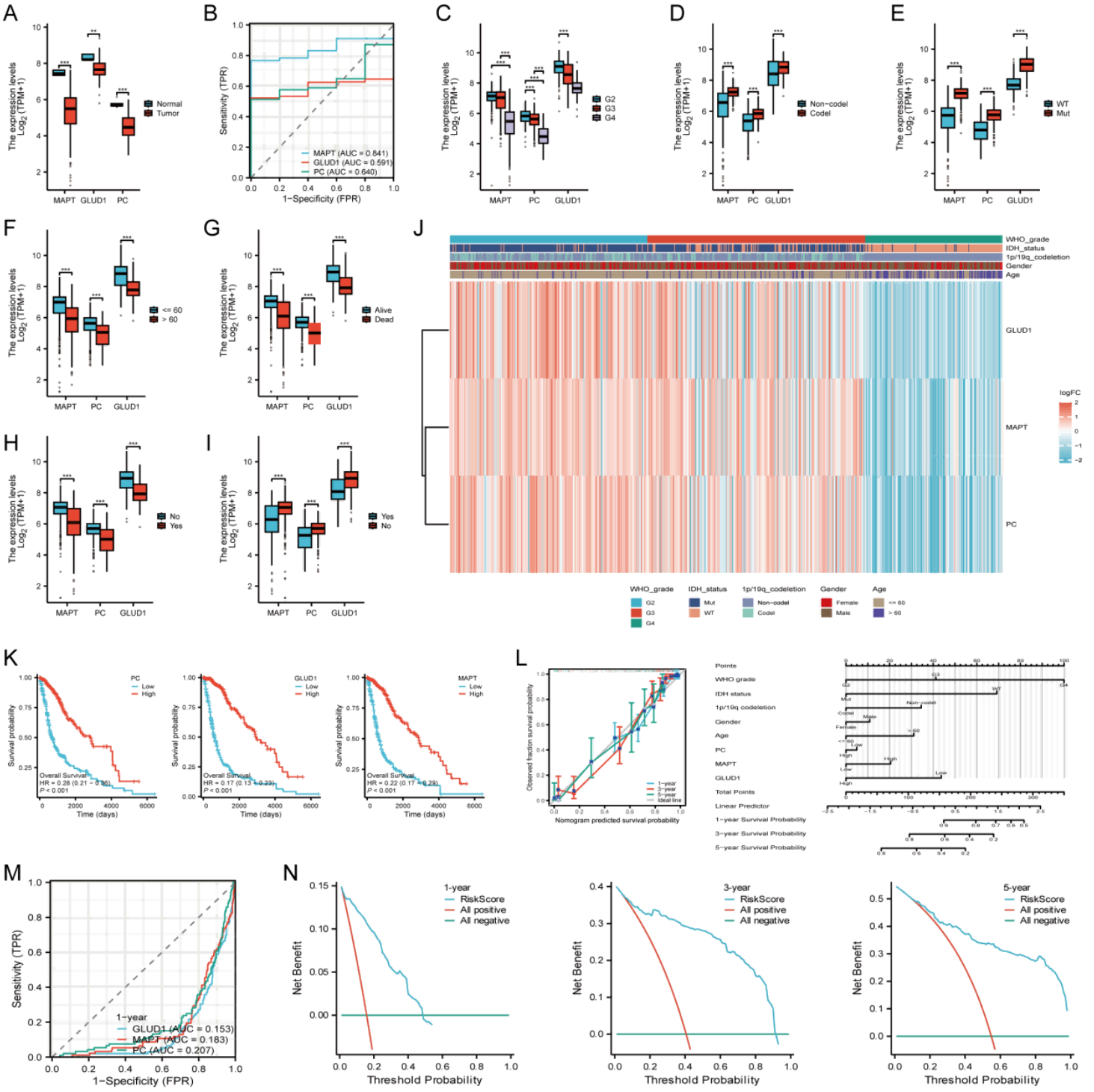


Figure 7

Expression patterns, clinicopathological associations, and exploratory prognostic evaluation of the MAPT-PC-GLUD1 signature in glioma.

(A) Boxplots showing that the mRNA expression levels of PC, GLUD1, and MAPT were significantly lower in glioma tissues than in normal brain tissues.

(B) ROC curves showing the discriminatory performance of PC, GLUD1, and MAPT in distinguishing glioma tissues from normal brain tissues.

(C) Scatter/box plots showing that the expression levels of PC, GLUD1, and MAPT progressively decreased with increasing WHO grade.

(D–F) Frequency plots showing that low expression of PC, GLUD1, and MAPT, defined according to the median expression value of each gene, was significantly associated with adverse clinicopathological features, including absence of 1p/19q codeletion (D), IDH wild-type status (E), and older age (> 60 years) (F).

(G–I) Associations between gene expression and clinical outcomes. Boxplots showing that, compared with the event-free group, the expression levels of PC, GLUD1, and MAPT were significantly lower in deceased patients (G), in patients with DSS events (H), and in patients with PFI events (I) ($P < 0.05$).

(J) Integrated heatmap showing the expression patterns of PC, GLUD1, and MAPT together with WHO grade, IDH status, age, sex, and 1p/19q status, highlighting expression-defined groups associated with different clinicopathological characteristics.

(K) Kaplan–Meier survival curves showing that patients with high expression of PC, GLUD1, or MAPT, defined according to the median expression value of each gene, had significantly longer overall survival than those with low expression ($P < 0.001$).

(L) Nomogram incorporating the expression status of the three genes together with WHO grade, IDH status, 1p/19q codeletion, sex, and age, along with calibration plots. The calibration curves showed agreement between nomogram-predicted and observed survival probabilities.

(M) ROC curves for 1-year mortality prediction based on PC (AUC = 0.207), GLUD1 (AUC = 0.153), and MAPT (AUC = 0.183). The AUC values below 0.5 indicate that these expression-based variables were inversely aligned with the risk definition used in this analysis and should therefore be interpreted with caution.

(N) DCA showing the performance of the nomogram across a range of threshold probabilities. The model showed comparative net benefit within specific threshold ranges in this dataset, particularly for predicting 3- and 5-year survival.

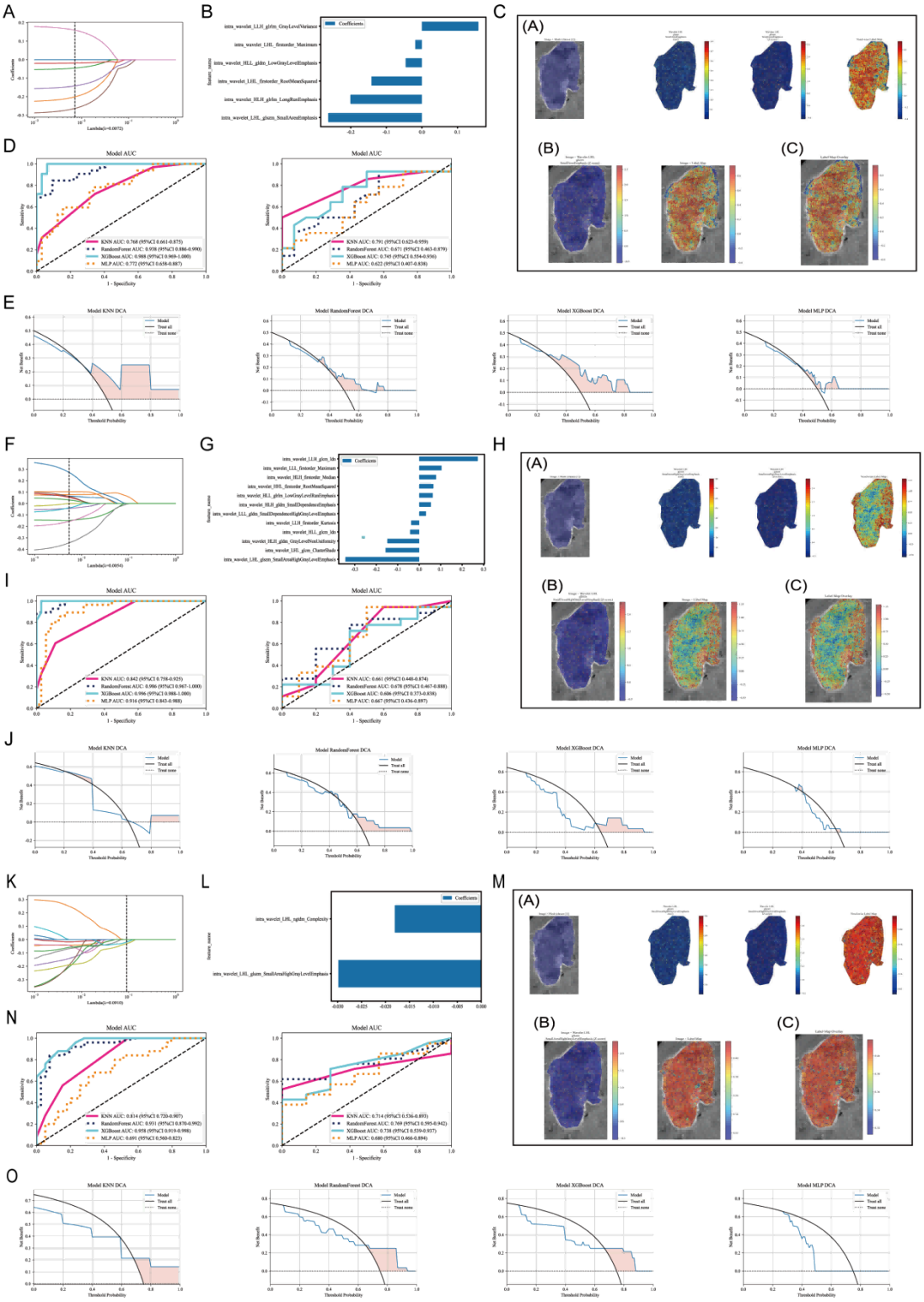


Figure 8

Feature selection, voxel-level radiogenomic mapping, and exploratory performance evaluation of radiomics models for PC, GLUD1, and MAPT expression levels.

This figure illustrates the radiomics workflow and predictive modeling results for three target genes: PC (A–E), GLUD1 (F–J), and MAPT (K–O).

(A, F, K) LASSO coefficient path plots for radiomic feature selection, showing the dimensionality reduction process for PC, GLUD1, and MAPT, respectively. Vertical dashed lines indicate the optimal log(λ) values determined by cross-validation.

(B, G, L) Bar plots showing the key radiomic features selected by LASSO and their corresponding regression coefficients.

(C, H, M) Voxel-level spatial mapping of tumor heterogeneity. Panels include the original MRI with ROI delineation, voxel-wise distribution maps of representative radiomic features, and fused prediction maps generated by the multivariate linear model.

(D, I, N) Receiver operating characteristic (ROC) curves showing the predictive performance of four machine learning classifiers (KNN, Random Forest, XGBoost, and MLP) in the training set (left) and internal validation set (right), with corresponding AUC values and 95% confidence intervals.

(E, J, O) DCA of the four classifiers in the internal validation set. The x-axis represents threshold probability, and the y-axis represents net benefit, illustrating the exploratory utility of each model across different risk thresholds.

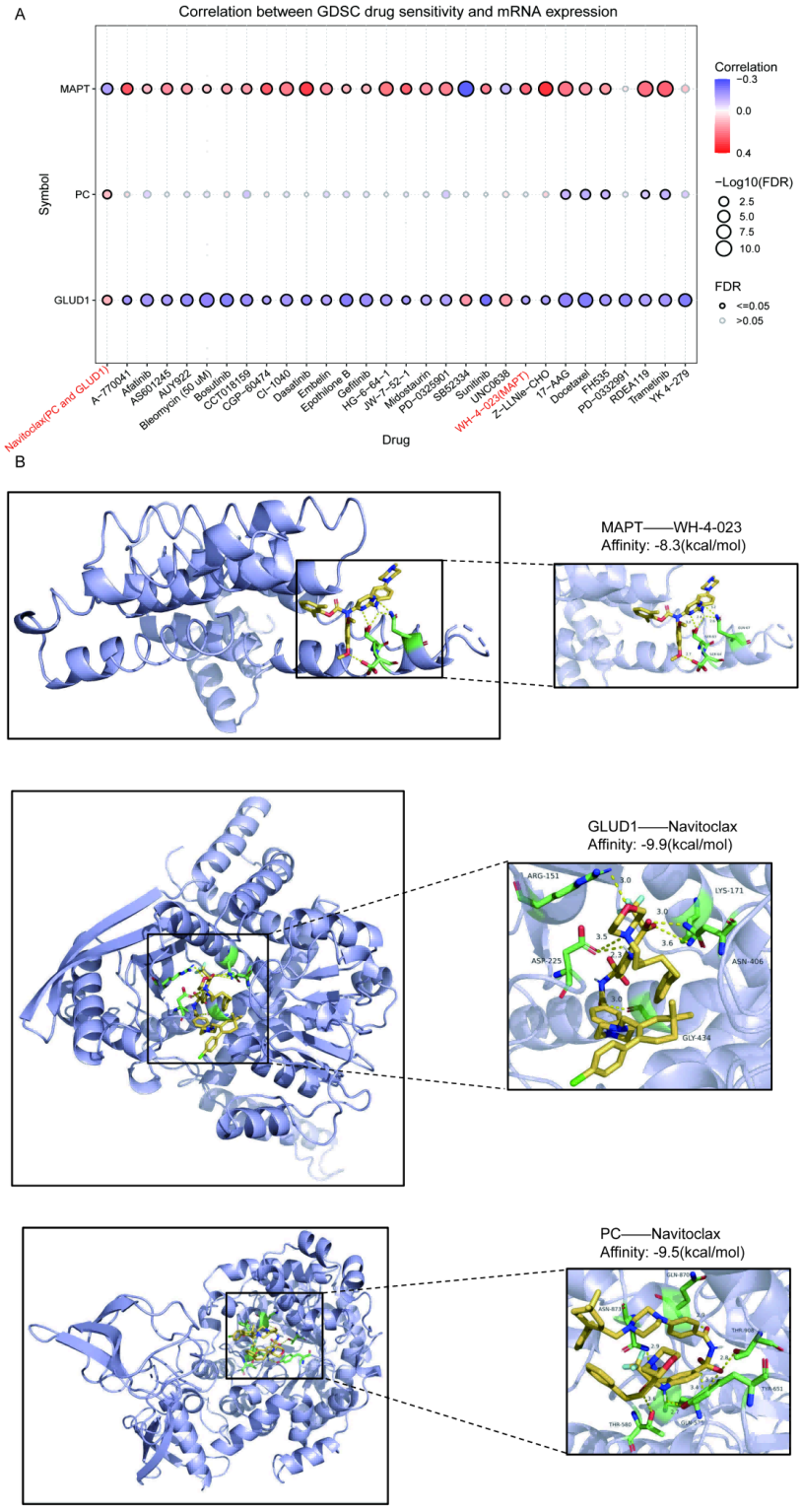


Figure 9

Exploratory identification of candidate therapeutic agents associated with PC, GLUD1, and MAPT.

(A) Correlation analysis between the expression levels of GLUD1, PC, and MAPT and drug sensitivity across 30 compounds. Increased expression of GLUD1 and PC was associated with enhanced

sensitivity to Navitoclax, whereas higher MAPT expression was associated with increased sensitivity to WH-4-023.

(B) Predicted binding mode of WH-4-023 with MAPT, showing a binding energy of −8.3 kcal/mol.

(C) Predicted docking pose of Navitoclax with GLUD1, with a binding energy of −9.9 kcal/mol.

(D) Predicted docking pose of Navitoclax with PC, with a binding energy of −9.5 kcal/mol.